Nanoscale

Volume 1 | Number 1 | Jan 2013 | Pages 1–100

Nanoscale

www.rsc.org/nanoscale

ROYAL SOCIETY OF CHEMISTRY

This is an *Accepted Manuscript*, which has been through the Royal Society of Chemistry peer review process and has been accepted for publication.

Accepted Manuscripts are published online shortly after acceptance, before technical editing, formatting and proof reading. Using this free service, authors can make their results available to the community, in citable form, before we publish the edited article. We will replace this *Accepted Manuscript* with the edited and formatted *Advance Article* as soon as it is available.

You can find more information about *Accepted Manuscripts* in the **Information for Authors**.

Please note that technical editing may introduce minor changes to the text and/or graphics, which may alter content. The journal's standard **Terms & Conditions** and the **Ethical guidelines** still apply. In no event shall the Royal Society of Chemistry be held responsible for any errors or omissions in this *Accepted Manuscript* or any consequences arising from the use of any information it contains.

ROYAL SOCIETY OF CHEMISTRY

www.rsc.org/nanoscale

High-Purity Iron Pyrite (FeS$_2$) Nanowires as High-Capacity Nanostructured Cathodes for Lithium-Ion Batteries

Linsen Li¶, Miguel Cabán-Acevedo¶, Steven N. Girard, and Song Jin*

Department of Chemistry, University of Wisconsin-Madison, 1101 University Avenue, Madison, Wisconsin 53706, United States

¶ These authors contributed equally to this work.

*E-mail: jin@chem.wisc.edu

Abstracts: Iron pyrite is an earth-abundant and inexpensive material that has long been interesting for electrochemical energy storage and solar energy conversion. A large-scale conversion synthesis of phase-pure pyrite nanowires has been developed for the first time. Nano-pyrite cathodes exhibited high Li-storage capacity and excellent capacity retention in Li/pyrite batteries using a liquid electrolyte, which retained a discharge capacity of 350 mAh g^{-1} and a discharge energy density of 534 Wh kg^{-1} after 50 cycles at 0.1 C rate.

Keywords: iron pyrite, nanowire, scalable synthesis, high-capacity cathode, lithium-ion battery

Iron pyrite (cubic FeS$_2$, fool's gold) has long been studied as an interesting material for solar energy conversion[1-4] and electrochemical energy storage[5-7]. Pyrite has a suitable band gap (E_g = 0.95 eV) and strong optical absorption ($\alpha > 6 \times 10^5$ cm^{-1} for $hv > 1.3$ eV), which stimulated the early research efforts in the 1980–1990s to investigate pyrite as a thin light absorber for photovoltaic (PV) and photoelectrochemical (PEC) applications.[1-4] Compared to other conventional leading solar materials such as Si and CdTe, pyrite stands out with its essentially limitless material abundance, low toxicity, and significantly lower raw material cost.[8] These

attractive attributes justify the resurgent interest in this material, as high-performance energy conversion devices based on inexpensive earth-abundant materials are favorable to address energy challenges today and for the future. It is comparatively less well known that pyrite is also an excellent and inexpensive battery cathode material that exhibits a high theoretical capacity of 894 mAh g^{-1} by reacting with four Li$^+$ *via* electrochemical conversion reaction to form Fe and Li$_2$S.[5, 9] It is currently used in commercial primary batteries and shows remarkable power performance and significantly longer working life than equivalent-sized alkaline batteries.[10] Pyrite has also been investigated as a promising secondary battery cathode in Li-Al/FeS$_2$ batteries for potential transport applications.[11, 12] It shows good reversibility at 400 °C[12] but only limited rechargeability can be achieved at ambient temperature[5]. Such limited reversibility is due in large part to the conversion mechanism involved in the lithiation/delithiation of pyrite cathodes, which operates very differently from the commonly used intercalation cathode materials.[9] To date, most of the previous pyrite cathodes were prepared from micrometer-sized natural[5, 6, 13-17] or synthetic[6, 13, 18] pyrite particles but the lithium-storage behavior of nanostructured phase-pure pyrite remains inadequately explored.

Nanostructuring has been shown as an effective approach to improve the capacity and rate capability of electrode materials by reducing the ion/electron diffusion distance, increasing electrode/electrolyte contact area, and better accommodating the strain associated with the lithium insertion/removal reaction.[19] This strategy has been much more prominently pursued for anode materials so far, such as Si[20-23] and Sn/SnO$_2$[24, 25], but it can be potentially more effective for conversion cathodes,[9, 26] such as pyrite, to address similar challenges including sluggish reaction kinetics and dramatic structural changes during lithiation and delithiation. However, the synthesis of phase-pure pyrite nanostructures has long been considered challenging. It is

complicated by the existence of many sub-stoichiometric iron sulfide phases and the polymorph marcasite phase (orthorhombic FeS_2).[2] Important advances have been made recently: a number of synthetic approaches to pyrite nanostructures have been reported, including chemical vapor deposition,[27-29] thermal sulfidation of iron,[30] sulfidation of Fe_2O_3 (hematite) assisted by a H_2S plasma,[31] sulfidation reaction with $FeCl_2$ or $FeBr_2$,[32] and colloidal nanocrystal synthesis.[33, 34] While these methods yield pyrite samples suitable for thin-film solar device fabrication and/or investigation of fundamental physical properties, the scale of these preparations is not sufficient (usually < 1 mg)[26-31] to allow battery electrode preparation. Chemical transformation of existing nanostructures provides a versatile approach to preparing novel nanomaterials and may potentially circumvent the aforementioned challenge. This approach not only allows independent control over the shape, size, morphology, structure and chemical composition of target materials, but may also enable scalable nanomaterial synthesis.[35] α-FeF_3·$3H_2O$ nanowires (NWs) can be synthesized from solution in a large quantity[36] and they are versatile precursors to make NWs of iron-based materials, such as α-Fe_2O_3 (hematite)[36] and iron fluoride (FeF_3)[26]. Here we report for the first time a scalable synthesis of phase-pure pyrite NWs *via* thermal sulfidation of the precursor α-FeF_3·$3H_2O$ NWs in bulk-like quantity. The phase purity of the converted pyrite NWs was confirmed by synchrotron-based high-resolution powder X-ray diffraction (HRPXRD), Raman spectroscopy, transmission electron microscopy (TEM), and electron diffraction (ED). Furthermore, we prepared composite electrodes comprised of pyrite NWs, carbon black, and polyvinylidene difluoride (PVDF) binder and performed galvanostatic cycling tests to show that the nano-pyrite cathodes exhibit high capacity and excellent capacity retention at room temperature. Note that in this work, we followed many previous literatures[5-7, 13-17] to describe and investigate our nano-pyrite as a cathode material, though pyrite has also been studied as an anode material in recent years[37-39]. Despite its lower potential (~1.5 V) compared with other

conventional intercalation cathodes, pyrite can provide a much higher Li-storage capacity of 894 mAh g^{-1}, assuming complete reaction to Li_2S and Fe. Therefore the theoretical energy density (the product of capacity and potential) of pyrite is still quite attractive. This is the reason we herein investigate pyrite as a cathode material and present the data in the context of a promising cathode materials.

To prepare the pyrite NWs, we first synthesized the precursor α-$FeF_3 \cdot 3H_2O$ NWs using a solution synthesis[36] that follows the design of dislocation-driven NW growth[40, 41] (see Supporting Information for experimental details). The α-$FeF_3 \cdot 3H_2O$ NWs were made in bulk-like white powders and first dried and partially dehydrated under vacuum. The color of the powders changed from white to brownish/greenish after the partial water loss. The pyrite NWs (~5−10 mg scale) were prepared by sulfidation of the partially dehydrated NWs at 500 °C for 2 h under a sulfur atmosphere using a home-made tube reactor equipped with gas-flow and pressure controls (Figure 1a). The sulfur precursor was positioned at a temperature of ~415 °C throughout the reaction, which yields an estimated sulfur vapor pressure of ~480 Torr[42]. The sulfidation of α-$FeF_3 \cdot 3H_2O$ NWs has also been accomplished in a closed ampoule using excess sulfur, which yields more pyrite sample in a single reaction batch (~50−80 mg scale). Representative scanning electron microscopy (SEM) images of the precursor α-$FeF_3 \cdot 3H_2O$ NWs (approximately 30−200 nm in diameter) and the as-converted pyrite NWs are shown in Figure 1b and 1c, respectively. The NWs became more tortuous after the sulfidation and tended to entangle and fuse to form mattes of NW networks (Figure 1c). The diameter of the pyrite NWs typically ranges from 15 nm to 200 nm.
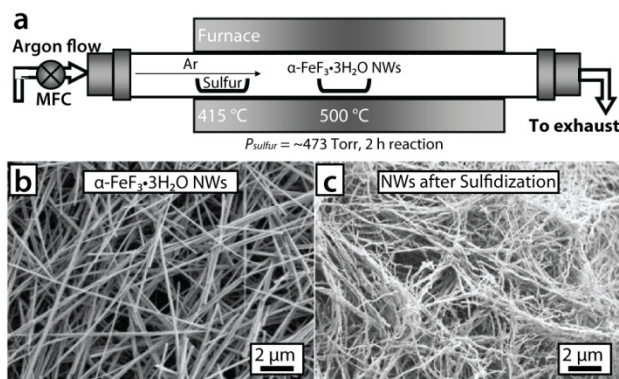
Figure 1. (a) Schematic illustration of the pyrite NW synthesis setup using a flow tube reactor; (b) and (c) are SEM images of the NWs before and after sulfidation.

The phase identity of the NWs after the sulfidation was confirmed to be pyrite (cubic FeS_2, JCPDS No. 65-3321, space group $Pa\overline{3}$, $a = 5.419$ Å) by synchrotron-based HRPXRD (Figure 2a) taken on beamline 11-BM at the Advanced Photon Source at Argonne National Laboratory. Even with the high 2θ range (25–155 °) and high sensitivity afforded by the HRPXRD, no other impurity phases such as marcasite (orthorhombic FeS_2, JCPDS No. 65-2567, space group $Pnnm$, $a = 4.445$ Å, $b = 5.425$ Å, $c = 3.388$ Å), pyrrhotite ($Fe_{1-x}S$, $x = 0$–0.17) , or troilite (FeS) were detectable. Furthermore, we have carried out confocal micro-Raman spectroscopy to provide additional evidence for the phase-purity of the converted NWs. A representative Raman spectrum (Figure 2b) shows three peaks at 339 cm^{-1}, 376 cm^{-1}, and 429 cm^{-1}, corresponding to three different characteristic active modes of pyrite, namely the S_2 libration (E_g), S-S in-phase stretch (A_g), and coupled libration and stretch [triplydegenerate, specifically $T_{g(3)}$] modes, respectively.[43, 44] No Raman peaks from marcasite (386 and 323 cm^{-1}) were observed.
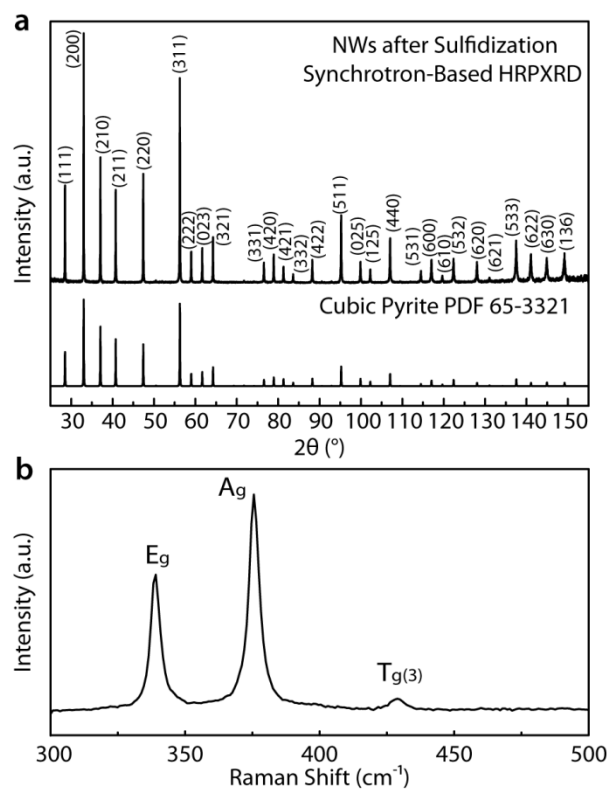
Figure 2. (a) HRPXRD of the NWs after sulfidation in comparison with reference diffractogram of cubic pyrite; (b) Confocal micro-Raman spectrum of the NWs after sulfidation.

The phase purity of the pyrite NWs was also investigated by TEM, ED, and fast Fourier transform (FFT) analysis. An ED ring pattern (Figure 3a) was obtained from an ensemble of NWs dropcasted on a TEM grid. The diffraction rings can be exclusively indexed to iron pyrite reflections. HRTEM was carefully performed and the representative HRTEM image (Figure 3b) shows a lattice-resolved single-crystal pyrite NW oriented along the [110] zone axis (ZA), determined from the corresponding indexed FFT (Figure 3b inset). Note that the zone axis patterns (ZAPs) of cubic pyrite and its orthorhombic polymorph marcasite are nearly identical and often difficult to conclusively distinguish due to their highly similar crystal structures. As we have demonstrated previously,[30, 32] HRTEM and FFT analysis must be carried out along unique ZAs of pyrite, such as [110] ZA, to convincingly identify the pyrite crystal structure and rule out

the existence of marcasite (see the comparison between the simulated [110] ZAP for pyrite and its

most similar ZAP for marcasite in Figure S1).
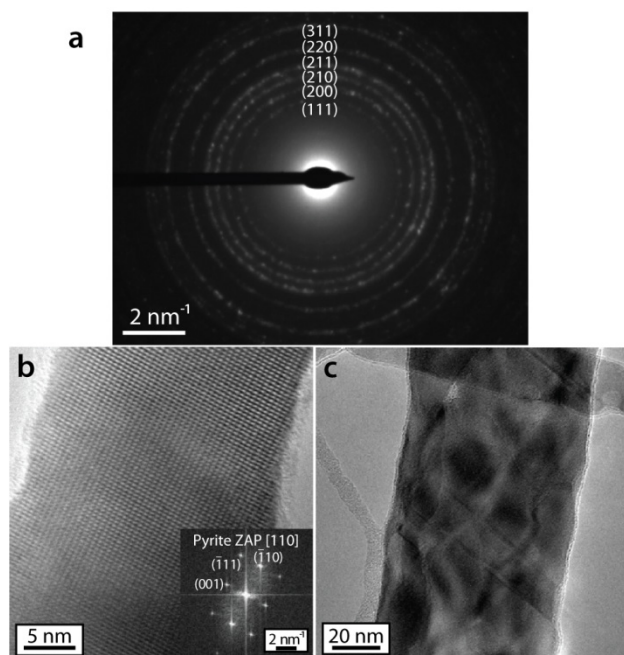
Figure 3. (a) Representative ED pattern for an ensemble of as-converted NWs revealing single-phase pyrite; (b) Lattice-resolved HRTEM image of a representative thin pyrite NW and the corresponding FFT showing its single crystallinity. Note that the [110] ZAP for pyrite is unique and distinguishable from any ZAPs for marcasite; (c) TEM image of a representative thick polycrystalline pyrite NW.

We have also examined the microstructure of the converted pyrite NWs using TEM and observed two types of structural transformation behavior correlated with the diameter of the NWs. Thinner pyrite NWs (typically < 20 nm in diameter) usually contains large segments of single crystalline pyrite domains or even exhibit complete single-crystallinity. One representative example is shown in Figure 3b, in which a continuous single-crystal pyrite lattice can be clearly seen. On the other hand, NWs with large diameters (typically > 20 nm) tend to become

polycrystalline. As shown in Figure 3c for a representative example, the NW is comprised of multiple polycrystalline domains, but the overall one-dimensional (1D) morphology after the sulfidation is preserved. The transformation behavior may be explained in terms of diffusion of reactant atoms/ions. For the thin NWs, smaller domain size and shorter diffusion distance may afford faster reaction kinetics. A single nucleation event of the pyrite phase likely occurs, which quickly propagates along the whole NW to achieve the homogeneous transformation with preserved single-crystallinity. Conversely, multiple nucleation events could occur in a thick NW and hence lead to the formation of polycrystalline pyrite domains. Similar chemical transforming behaviors have been observed in the conversion of α-FeF$_3$·3H$_2$O NWs to α-Fe$_2$O$_3$ NWs, though the critical diameter for the preservation of single-crystallinity is larger (~100 nm) in that case.[36] These two syntheses decouple the control over material morphology and chemical composition and produce iron-based functional nanomaterials in a large quantity, which further illustrates that the chemical transformation of existing nanostructures is a versatile method of nanomaterial synthesis,[35] and specifically, α-FeF$_3$·3H$_2$O NWs are very useful precursors to NWs of other iron-based nanomaterials.

We suggest that the following chemical reactions may be responsible for the conversion of the NWs, in which partially dehydrated α-FeF$_3$·3H$_2$O (FeF$_3$·xH$_2$O) quickly loses the residual lattice water and reacts with sulfur vapor to produce pyrite and sulfur hexafluoride (SF$_6$) at 500 °C.

$$4\text{FeF}_3 \cdot x\text{H}_2\text{O } (s) + 5\text{S}_2 (g) \rightarrow 4\text{FeS}_2 (s) + 2\text{SF}_6 (g) + 4x\text{H}_2\text{O } (g) \quad (1)$$

This is the first investigation of chemical transformation of iron fluoride to iron pyrite. The conversion is favorable because both pyrite and SF$_6$ are very stable (see estimated Gibbs free

energy of formation in Table S1) in the sulfur-rich atmosphere at the reaction temperature (500

°C) and the volatile products (SF_6 and water vapor) are quickly carried away by the flowing argon

gas, driving the equilibrium to favor the formation of pyrite based on Le Chatelier's principle.

Furthermore, benefited from the metastability and nanoscale dimension of the precursor NWs, the

kinetic energy barrier for atoms and ions to diffuse is significantly reduced. This effectively

facilitates in the complete conversion from the iron fluoride precursor to pyrite without producing

any other iron sulfide impurities, such as pyrrhotite $Fe_{1-x}S$ and marcasite FeS_2. Compared with

previous pyrite synthesis, the facile conversion reported herein not only produces phase-pure

pyrite, it is also significantly larger in reaction scale, which greatly facilitates our subsequent

study on the lithium-storage capability of nanostructured pyrite cathodes.

We have also measured the optical absorption of the as-synthesized pyrite NWs using a UV-

Vis-NIR spectrophotometer equipped with an integration sphere. The pyrite NW film (~500 nm

in thickness) deposited on a borosilicate glass substrate shows very strong optical absorption ($\alpha >$

10^5 cm^{-1} for $hv > 1.0$ eV) and an absorption onset of about ~0.8 eV. More precise determination

of the optical bandgap is complicated by the existence of sub-band gap absorption, which is often

observed on nanostructured pyrite samples[31, 45] but its origin is still controversial and requires

further investigation. The strong light absorption of the pyrite NWs illustrates that they can be

effective solar absorber. Therefore, we have prepared semiconducting pyrite thin-film electrodes

by converting α-FeF$_3\cdot$3H$_2$O NW films deposited on conductive substrates[46]. Investigation of their

photoelectrochemical properties is underway.
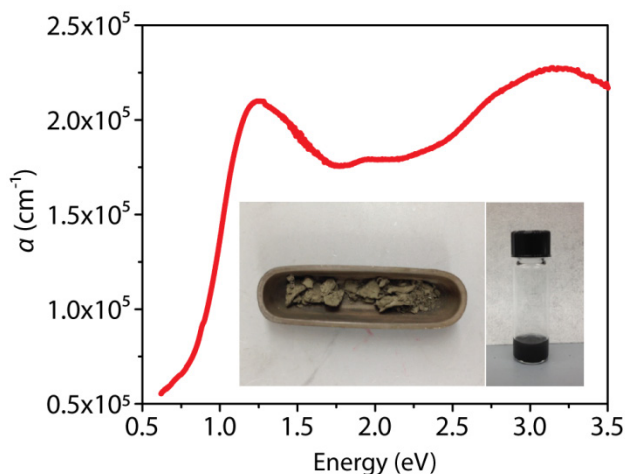
Figure 4. Absorption coefficient α of a pyrite NW film (~500 nm in thickness) deposited on a borosilicate glass substrate. α may be underestimated due to the void spaces within the NW film. Insets show the appearance of the converted pyrite NWs (about 45 mg in an alumina boat of 3 cm in length) and a NW/iso-propanol suspension, demonstrating that the pyrite NWs absorb light strongly.

We performed electrochemical tests on composite electrodes made of pyrite NWs, carbon black, and PVDF binder in a weight ratio of 7:2:1 packed into coin cells (see Supporting Information for details). As the highly entangled and fused pyrite NWs could be broken into shorter nanorods and small nanoparticles during the electrode preparation process, we refer to the as-prepared composite electrodes as nano-pyrite cathodes and do not judge how the NW morphology affects the electrochemical performance in this work. 1 M lithium bis(trifluoromethane)sulfonimide (LiTFSi) dissolved in tetra(ethylene glycol)dimethyl ether (TEGDME) was used as the battery electrolyte, because it was shown to improve the cycling performance of Li/FeS$_2$ batteries at room temperature as compared to the more common ethylene carbonate/dimethyl carbonate based electrolytes.[16] We will focus our discussion on the lithium storage behavior of nanostructured pyrite.

We first investigated the lithium storage behavior of the nano-pyrite cathode in the 1st discharge at different current densities. Four Li/nano-pyrite cells were discharged from open-circuit voltage to 1.1 V at 0.01 C, 0.05 C, 0.1 C, and 0.2 C (1 C = 894 mA g^{-1} for pyrite) rate respectively and their discharge profiles are shown in Figure 4a. The nano-pyrite cathode exhibited a high discharge capacity of 744 mAh g^{-1} at 0.01 C rate, which is equivalent to ~3.3 Li^+ storage per FeS_2 (Figure 5a). When we lower the cut-off voltage to 0.9 V, ~3.6 Li+ storage per FeS_2 (~800 mAh g^{-1}) can be achieved. This performance is comparable to those obtained on the best FeS_2 cathodes reported previously.[13, 14] According to previous work,[5] the lithiation of pyrite involves two reactions, which can occur at one or two voltage depending on the kinetics of the system.

$$FeS_2 + 2Li^+ + 2e^- \rightarrow Li_2FeS_2 \quad (2)$$

$$Li_2FeS_2 + 2Li^+ + 2e^- \rightarrow 2Li_2S + Fe^0 \quad (3)$$
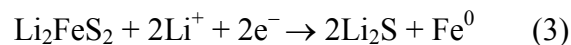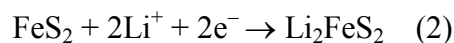
At ambient temperature (T ≤ 30 °C), the two reactions proceed simultaneously due to the slow diffusion of Li^+ into pyrite, which explains the single plateau at ~1.53 V observed in this work (Figure 5a) and other reports.[5, 6, 13-16] Using electrochemical impedance spectroscopy (see Figure S2 for details), we estimated that the diffusion coefficient of Li^+ of the nano-pyrite cathodes were on the order of 10^{-14}–10^{-15} cm^2 s^{-1}. Note that at higher temperatures (T > 55 °C) the rate of diffusion of Li^+ through the bulk pyrite increases and the first reaction could proceed at a higher voltage of ~1.7 V.[5] We also observed that the discharge capacity and voltage plateau of nano-pyrite cathode are rate dependent. When the discharge current density increases, the discharge capacity decreases and the plateau voltage drops slightly. For example, at a rate of 0.2 C, the nano-pyrite cathode yielded a lower capacity of 651 mAh g^{-1} with a lower voltage plateau of

~1.42 V (Figure 5a). At high current densities, this effect originates from the slow Li$^+$ diffusion within the electrode and/or across an electrode/electrolyte interface that hinders charge distribution to reach equilibrium.[47] The accumulated Li$^+$ and electrons at the electrode surface force the formation of most Li-rich phases (Li$_2$S and Fe). Hence the battery voltage drops faster and the discharge process is also terminated faster, even though the inner part of electrode material has not been fully utilized.
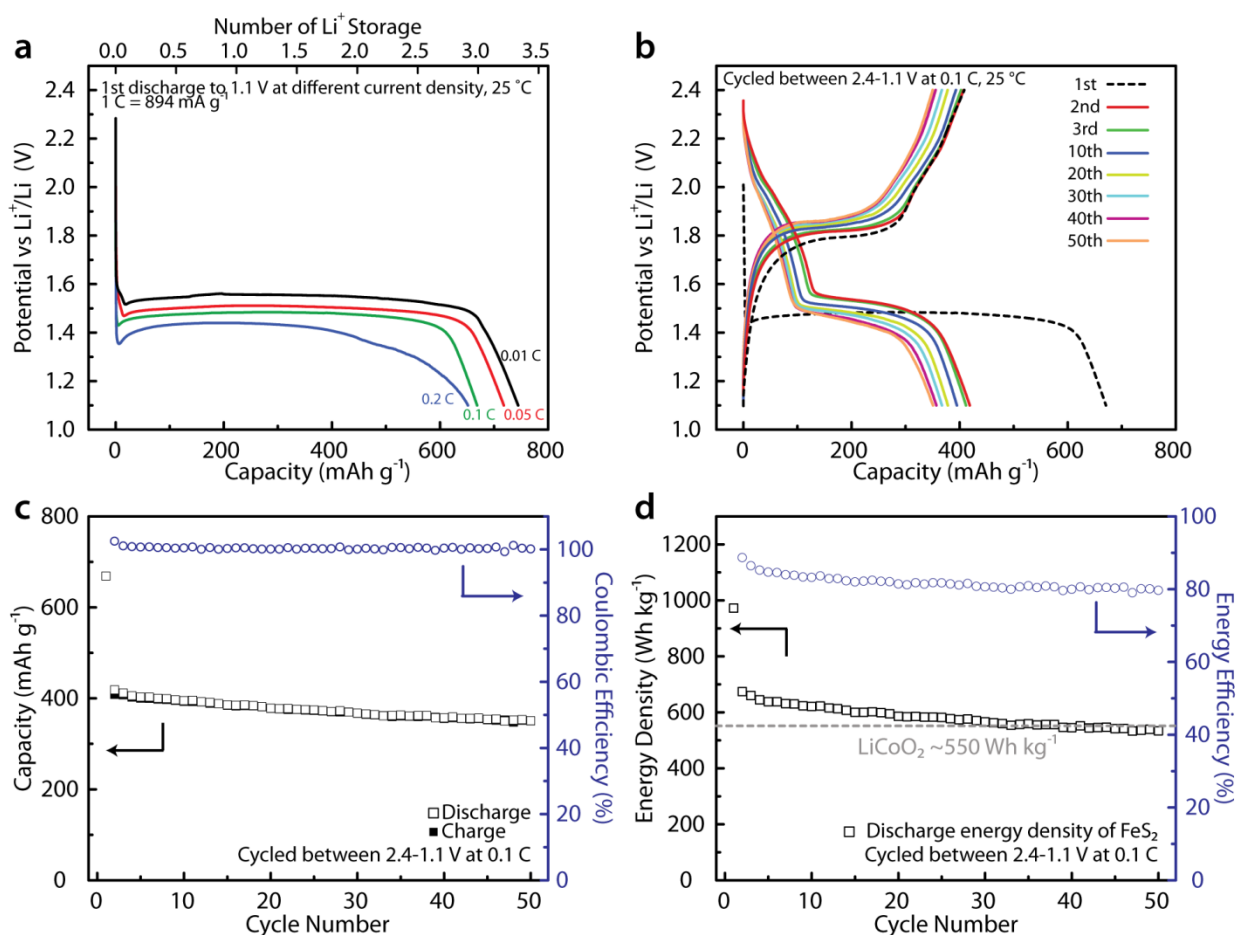
Figure 5. (a) Discharge profiles of four different Li/nano-pyrite cells discharge at different current densities at room temperature; (b) Voltage profiles for the 1st, 2nd, 3rd, 10th, 20th, 30th, 40th, and 50th discharge-charge cycles of a nano-pyrite cathode cycled between 2.4−1.1 V at 0.1 C rate at room temperature; (c) Discharge/charge capacity and Coulombic efficiency of the same

nano-pyrite cathode in (b) vs cycle number. Note that the FeS_2 cathode is initially at charged state

and undergoes discharging at the 1st cycle so that CE is only calculated from the 2nd cycle to the

50th cycle. The Coulombic efficiencies are slightly higher than 100%, which could be due to

minor side reactions during discharge; (d) Discharge energy density and energy efficiency of the

nano-pyrite cathode vs cycle number shown along with the theoretical discharge energy density

of $LiCoO_2$ cathode (550 Wh kg^{-1} based on the mass of $LiCoO_2$ only), which is calculated using

an average voltage of 3.9 V and a capacity of 140 mAh g^{-1}. Note that all the reported capacity

performance in this paper was calculated based on the mass of the FeS_2. The energy density of

the whole battery can be diluted ~4–5 times when the mass of all other battery components is

considered

    We further investigated the reversible lithium storage capability of the nano-pyrite cathode

using discharge/charge cycling tests. The Li/nano-pyrite cell was cycled over the voltage range of

2.4–1.1 V *vs* Li^+/Li at 0.1 C rate. The nano-pyrite cathode exhibited a discharge capacity of 668

mAh g^{-1} at the 1st discharge but only 409 mAh g^{-1} was recovered at the subsequent charge

(Figure 5b, dashed curves). Despite this, the nano-pyrite cathode showed a very stable cycling

performance after the first cycle (Figure 5c). It retained a discharge capacity of 350 mAh g^{-1} after

50 cycles and showed high averge Coulombic efficiency (100.4%, Figure 5c). The Li-storage

capacity of the nano-pyrite cathode is much higher than that of the current $LiCoO_2$ intercalation

cathode material (140 mAh g^{-1}). This enables the nano-pyrite cathode to have comparable

discharge energy density to the theoretical energy density of $LiCoO_2$ cathode (Figure 5d) in spite

of its lower potential. To the best of our knowledge, such good cycling performance of a Li/FeS_2

cell using a liquid electrolyte at room temperature has not been reported before. The good

performance may be attributed to the nanoscale dimension of the nano-pyrite cathode, which

affords a shorter Li^+ and electron transport pathway, improved conversion reaction kinetics, and better utilization of the active material upon discharge and charge.

Our results demonstrate that nanostructured pyrite can be a promising cathode material to enable high-capacity rechargeable batteries at lower material cost. However, since the charge capacity is only ~61 % of the discharge capacity in the first cycle, it is clear that the pyrite phase is not recovered upon recharge to 2.4 V and the full capacity of pyrite cathode is not yet utilized in subsequent cycling. Previous reports[5, 15, 18] suggest that the most probable phase formed in the charge reaction and also the most relevant electrochemically active phase in subsequent cycling could be $Li_{2-x}FeS_2$ $(0 < x < 0.8)$:

Charge reactions:

$$Fe^0 + 2Li_2S \rightarrow Li_2FeS_2 + 2Li^+ + 2e^- \quad (4)$$

$$Li_2FeS_2 \rightarrow Li_{2-x}FeS_2 + xLi^+ + xe^- \ (0 < x < 0.8) \quad (5)$$

Subsequent cycling:

$$Li_{2-x}FeS_2 + (2+x)Li^+ + (2+x)\ e^- \rightleftarrows Fe^0 + 2Li_2S \ (0 < x < 0.8) \quad (6)$$
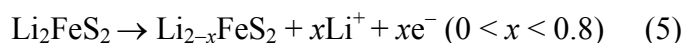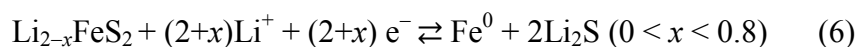
As Fe^0 is involved in the discharge and charge reactions, the cycling behavior of such electrode is different from that of a pure Li_2S cathode, which shows different voltage profile and usually suffers rapid capacity loss.[48] We have also measured a cyclic voltammogram of a nano-pyrite cathode cycled between 2.4 V and 0.7 V vs Li^+/Li. The result is consistent with our discussion above and previous reports[5, 15] (see Figure S3 for details).

In order to recover the pyrite phase and obtain more capacity, we have tried to recharge the Li/nano-pyrite cell to a higher voltage (> 2.4 V), but such attempts resulted in fast capacity fading

14

(Figure S4) in subsequent cycles. Previous *in situ* X-ray diffraction and *in situ* Mössbauer spectroscopy studies on micrometer-sized pyrite cathodes have shown that upon recharge to beyond 2.4 V, the hexagonal $Li_{2-x}FeS_2$ phase ($0 < x < 0.8$) formed in the charge reaction begins to decompose to form non-stoichiometric pyrrhotite (FeS_y) and elemental sulfur (S):[5]

$$Li_{2-x}FeS_2 \rightarrow FeS_y + (2-y)S + (2-x)Li^+ + (2-x)e^- \quad (7)$$
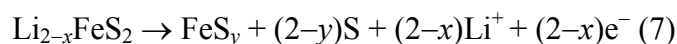
As these two phases (FeS_y and S) do not readily react to produce pyrite at temperatures below 265 °C,[5] lithiation of elemental sulfur occurs in the subsequent discharge (Figure S4) to produce a large amount of lithium sulfides likely isolated from the active Fe nanodomains formed in the discharge reaction. As the large amount of interfacial surface between lithium sulfide and Fe nanodomains is the key to the reversibility of their conversion reactions,[9, 18] isolated lithium sulfides are difficult to decompose during recharge and could dissolve more easily in the liquid electrolyte. This provides an possible explanation for the observed fast capacity fading (Figure S4). Therefore, we suggest that simply nanostructuring the pyrite cathode is not sufficient to fully address the challenge facing room-temperature Li/FeS_2 batteries using a liquid electrolyte. In order to fully utilize the charge-storage capability of pyrite, the incorporation of carefully designed catalysts may be necessary to alter the reaction pathway and suppress the formation of elemental sulfur during recharge.[9] *In situ* TEM[49] or *in situ* transmission X-ray microscopy[50, 51] studies on the electrochemical conversion reactions of single-crystal pyrite NWs[32] may also be a fruitful future direction to provide insights into the reaction mechanism at the microscopic level.

In summary, we have demonstrated the first example of large-scale synthesis of pyrite NWs *via* chemical transformation of iron fluoride NWs. As conclusively confirmed by various structural characterization techniques, high-purity pyrite NWs without other lower sulfides or marcasite polymorph impurities can be readily produced by this conversion synthesis. The

nanostructured pyrite cathode prepared from the pyrite NWs exhibited excellent cycling performance at room temperature over the voltage range of 2.4–1.1 V in a Li/FeS_2 cell using a 1 M LiTFSi/TEGDME electrolyte, which retained a discharge capacity of 350 mAh g^{-1} after 50 cycles at 0.1 C rate. Furthermore, we revealed that nanostructuring did improve the reaction kinetics by shortening the Li^+ and electron transport path but it likely has not altered the delithiation reaction pathway. This work establishes nanostructured pyrite as a promising high-capacity cathode materials for rechargeable Li-ion batteries. In order to fully utilize the charge storage capability of pyrite, more in-depth understanding of the electrochemical conversion mechanism *via in situ* microscopy studies and additional strategies to control the conversion reactions such as incorporating carefully designed catalysts are needed. We hope that this work can serve as an impetus for further research efforts aiming to utilize earth-abundant Fe-based conversion cathode materials to increase the energy storage of Li-ion batteries.

Electronic Supplementary Information (ESI) available: Experimental details, estimated Gibbs energy of formation of pyrite and SF_6, a comparison between the simulated [110] ZAP for pyrite and its most similar ZAP for marcasite, measurements of diffusion coefficients of lithium ions, cyclic voltammogram of a nano-pyrite cathode, and a voltage profile of a Li/nano-pyrite cell cycled in 2.5–1.1 V. See DOI: 10.1039/c000000x/

Acknowledgements

Nanoscale Accepted Manuscript

References

1. A. Ennaoui, and H. Tributsch. *Solar Cells* **1984,** 13, 197-200.
2. A. Ennaoui,S. Fiechter,C. Pettenkofer,N. Alonso-Vante,K. Büker,M. Bronold,C. Höpfner, and H. Tributsch. *Sol. Energy Mater. Sol. Cells* **1993,** 29, 289-370.
3. A. Ennaoui,S. Fiechter,H. Goslowsky, and H. Tributsch. *J. Electrochem. Soc.* **1985,** 132, 1579-1582.
4. A. Ennaoui, and H. Tributsch. *Sol. Energy Mater.* **1986,** 14, 461-474.
5. R. Fong,J. R. Dahn, and C. H. W. Jones. *J. Electrochem. Soc.* **1989,** 136, 3206-3210.
6. Y. Shao-Horn, and Q. C. Horn. *Electrochim. Acta* **2001,** 46, 2613-2621.
7. E. Peled,D. Golodnitsky,E. Strauss,J. Lang, and Y. Lavi. *Electrochim. Acta* **1998,** 43, 1593-1599.
8. C. Wadia,A. P. Alivisatos, and D. M. Kammen. *Environ. Sci. Techno.* **2009,** 43, 2072-2077.
9. J. Cabana,L. Monconduit,D. Larcher, and M. R. Palacin. *Adv. Mater.* **2010,** 22, E170-E192.
10. *Engergizer Lithium Iron Disulfide Batteries, Handbook and Application Manual, http://data.energizer.com/PDFs/lithiuml91l92_appman.pdf*.
11. Z. Tomczuk,B. Tani,N. C. Otto,M. F. Roche, and D. R. Vissers. *J. Electrochem. Soc.* **1982,** 129, 925-931.
12. S. K. Preto,Z. Tomczuk,S. v. Winbush, and M. F. Roche. *J. Electrochem. Soc.* **1983,** 130, 264-273.
13. Y. Shao-Horn,S. Osmialowski, and Q. C. Horn. *J. Electrochem. Soc.* **2002,** 149, A1499-A1502.
14. Y. Shao-Horn,S. Osmialowski, and Q. C. Horn. *J. Electrochem. Soc.* **2002,** 149, A1547-A1555.
15. Y. J. Choi,N. W. Kim,K. W. Kim,K. K. Cho,G. B. Cho,H. J. Ahn,J. H. Ahn,K. S. Ryu, and H. B. Gu. *J. Alloy. Compd.* **2009,** 485, 462-466.
16. J. W. Choi,G. Cheruvally,H. J. Ahn,K. W. Kim, and J. H. Ahn. *J. Power Sources* **2006,** 163, 158-165.
17. L. A. Montoro,J. M. Rosolen,J. H. Shin, and S. Passerini. *Electrochim. Acta* **2004,** 49, 3419-3427.
18. T. A. Yersak,H. A. Macpherson,S. C. Kim,V.-D. Le,C. S. Kang,S.-B. Son,Y.-H. Kim,J. E. Trevey,K. H. Oh,C. Stoldt, and S.-H. Lee. *Adv. Energy Mater.* **2012,** 3, 120-127.
19. P. G. Bruce,B. Scrosati, and J.-M. Tarascon. *Angew. Chem. Int. Ed.* **2008,** 47, 2930-2946.
20. C. K. Chan,H. Peng,G. Liu,K. McIlwrath,X. F. Zhang,R. A. Huggins, and Y. Cui. *Nat. Nanotech.* **2008,** 3, 31-35.

21. H. Wu,G. Chan,J. W. Choi,I. Ryu,Y. Yao,M. T. McDowell,S. W. Lee,A. Jackson,Y. Yang,L. Hu, and Y. Cui. *Nat. Nanotech.* **2012,** 7, 310-315.

22. H. Wu,G. Yu,L. Pan,N. Liu,M. T. McDowell,Z. Bao, and Y. Cui. *Nat. Commun.* **2013,** 4, 1943.

23. J. R. Szczech, and S. Jin. *Energy & Environ. Sci.* **2011,** 4, 56-72.

24. X. W. Lou,C. M. Li, and L. A. Archer. *Adv. Mater.* **2009,** 21, 2536-2539.

25. X. W. Lou,Y. Wang,C. L. Yuan,J. Y. Lee, and L. A. Archer. *Adv. Mater.* **2006,** 18, 2325-2329.

26. L. Li,F. Meng, and S. Jin. *Nano Lett.* **2012,** 12, 6030-6037.

27. B. Meester,L. Reijnen,A. Goossens, and J. Schoonman. *Chem. Vap. Depos.* **2000,** 6, 121-128.

28. C. Höpfner,K. Ellmer,A. Ennaoui,C. Pettenkofer,S. Fiechter, and H. Tributsch. *J. Crystal Growth* **1995,** 151, 325-334.

29. N. Berry,M. Cheng,C. L. Perkins,M. Limpinsel,J. C. Hemminger, and M. Law. *Adv. Energy Mater.* **2012,** 2, 1124-1135.

30. M. Cabán-Acevedo,M. S. Faber,Y. Tan,R. J. Hamers, and S. Jin. *Nano Lett.* **2012,** 12, 1977-1982.

31. R. Morrish,R. Silverstein, and C. A. Wolden. *J. Am. Chem. Soc.* **2012,** 134, 17854-17857.

32. M. Cabán-Acevedo,D. Liang,K. S. Chew,J. P. DeGrave,N. S. Kaiser, and S. Jin. *ACS Nano* **2013,** 7, 1731-1739.

33. C. Wadia,Y. Wu,S. Gul,S. K. Volkman,J. Guo, and A. P. Alivisatos. *Chem. Mater.* **2009,** 21, 2568-2570.

34. J. Puthussery,S. Seefeld,N. Berry,M. Gibbs, and M. Law. *J. Am. Chem. Soc.* **2010,** 133, 716-719.

35. G. D. Moon,S. Ko,Y. Min,J. Zeng,Y. Xia, and U. Jeong. *Nano Today* **2011,** 6, 186-203.

36. L. Li,Y. Yu,F. Meng,Y. Tan,R. J. Hamers, and S. Jin. *Nano Lett.* **2012,** 12, 724-731.

37. D. Zhang,Y. J. Mai,J. Y. Xiang,X. H. Xia,Y. Q. Qiao, and J. P. Tu. *J. Power Sources* **2012,** 217, 229-235.

38. D. Zhang,X. L. Wang,Y. J. Mai,X. H. Xia,C. D. Gu, and J. P. Tu. *J Appl. Electrochem.* **2012,** 42, 263-269.

39. J. Xia,J. Jiao,B. Dai,W. Qiu,S. He,W. Qiu,P. Shen, and L. Chen. *RSC Advances* **2013,** 3, 6132-6140.

40. S. Jin,M. J. Bierman, and S. A. Morin. *J. Phys. Chem. Lett.* **2010,** 1, 1472-1480.

41. S. A. Morin,M. J. Bierman,J. Tong, and S. Jin. *Science* **2010,** 328, 476-480.

42. D.-Y. Peng, and J. Zhao. *J. Chem. Thermodyn.* **2001,** 33, 1121-1131.

43. A. K. Kleppe, and A. P. Jephcoat. *Mineralogical Magazine* **2004,** 68, 433-441.

44. H. Vogt,T. Chattopadhyay, and H. J. Stolz. *J. Phys. Chem. Solids* **1983,** 44, 869-873.

45. Y. Bi,Y. Yuan,C. L. Exstrom,S. A. Darveau, and J. Huang. *Nano Lett.* **2011,** 11, 4953-4957.

46. M. S. Faber,K. Park,M. Cabán-Acevedo,P. K. Santra, and S. Jin. *J. Phys. Chem. Lett.* **2013,** 4, 1843-1849.

47. J. B. Goodenough, and Y. Kim. *Chem. Mater.* **2009,** 22, 587-603.

48. K. Cai,M.-K. Song,E. J. Cairns, and Y. Zhang. *Nano Lett.* **2012,** 12, 6474-6479.

49. F. Wang,H.-C. Yu,M.-H. Chen,L. Wu,N. Pereira,K. Thornton,A. Van der Ven,Y. Zhu,G. G. Amatucci, and J. Graetz. *Nat. Commun.* **2012,** 3, 1201.

50. J. Nelson,S. Misra,Y. Yang,A. Jackson,Y. Liu,H. Wang,H. Dai,J. C. Andrews,Y. Cui, and M. F. Toney. *J. Am. Chem. Soc.* **2012,** 134, 6337-6343.

51. F. Meirer,J. Cabana,Y. Liu,A. Mehta,J. C. Andrews, and P. Pianetta. *J. Synchroton Radiat.* **2011,** 18, 773-781.

Table of contents entry: Iron pyrite is an earth-abundant and inexpensive material that has long been interesting for electrochemical energy storage and solar energy conversion. A large-scale conversion synthesis of phase-pure pyrite nanowires has been developed for the first time. Nano-pyrite cathodes exhibit high Li-storage capacity and excellent capacity retention, which demonstrates the promise of pyrite nanomaterials as a cost-effective high-capacity cathode material for Li-ion batteries.

Table of Content Figure: